Ultrasonics Sonochemistry 38 (2017) 256–270

Contents lists available at ScienceDirect

Ultrasonics Sonochemistry

journal homepage: www.elsevier.com/locate/ultson

Structural evolution, growth mechanism and photoluminescence properties of $CuWO_4$ nanocrystals

E.L.S. Souza [a], J.C. Sczancoski [b], I.C. Nogueira [c], M.A.P. Almeida [d], M.O. Orlandi [e], M.S. Li [f], R.A.S. Luz [a], M.G.R. Filho [a], E. Longo [e], L.S. Cavalcante [a,*]

[a] PPGQ-CCN-GERATEC, Universidade Estadual do Piauí, Rua: João Cabral, N. 2231, P.O. Box 381, 64002-150 Teresina, PI, Brazil
[b] DQ-UFSCar, Universidade Federal de São Carlos, P.O. Box 676, São Carlos, SP 13565-905, Brazil
[c] ICE-Universidade Federal do Amazonas, Av. Rodrigo Otávio Japiim, P.O. Box 670, 69077-000 Manaus, AM, Brazil
[d] CCT-Universidade Federal do Maranhão, P.O. Box 322, 65080-805 São Luís, MA, Brazil
[e] Departamento de Físico-Química, Universidade Estadual Paulista, 14800-060 Araraquara, SP, Brazil
[f] IFSC-Universidade de São Paulo, P.O. Box 369, 13560-970 São Carlos, SP, Brazil

ARTICLE INFO

Article history:
Received 31 January 2017
Received in revised form 6 March 2017
Accepted 6 March 2017
Available online 8 March 2017

Keywords:
$CuWO_4$ crystals
Sonochemistry
Clusters
Raman spectroscopy
TEM images
Photoluminescence properties

ABSTRACT

Copper tungstate ($CuWO_4$) crystals were synthesized by the sonochemistry (SC) method, and then, heat treated in a conventional furnace at different temperatures for 1 h. The structural evolution, growth mechanism and photoluminescence (PL) properties of these crystals were thoroughly investigated. X-ray diffraction patterns, micro-Raman spectra and Fourier transformed infrared spectra indicated that crystals heat treated and 100 °C and 200 °C have water molecules in their lattice (copper tungstate dihydrate ($CuWO_4{\cdot}2H_2O$) with monoclinic structure), when the crystals are calcinated at 300 °C have the presence of two phase ($CuWO_4{\cdot}2H_2O$ and $CuWO_4$), while the others heat treated at 400 °C and 500 °C have a single $CuWO_4$ triclinic structure. Field emission scanning electron microscopy revealed a change in the morphological features of these crystals with the increase of the heat treatment temperature. Transmission electron microscopy (TEM), high resolution-TEM images and selected area electron diffraction were employed to examine the shape, size and structure of these crystals. Ultraviolet–Visible spectra evidenced a decrease of band gap values with the increase of the temperature, which were correlated with the reduction of intermediary energy levels within the band gap. The intense photoluminescence (PL) emission was detected for the sample heat treat at 300 °C for 1 h, which have a mixture of $CuWO_4{\cdot}2H_2O$ and $CuWO_4$ phases. Therefore, there is a synergic effect between the intermediary energy levels arising from these two phases during the electronic transitions responsible for PL emissions.

1. Introduction

Hydrous copper tungstate ($CuWO_4{\cdot}xH_2O$) crystals can be naturally found as a mineral, presenting colors from bright yellowish to green [1]. This mineral, also known as "*Cuprotungstite*", has been discovered and analyzed by Whitney T. Schaller in 1892. However, the same designation also is adopted for copper tungstate ($CuWO_4$), i.e., an oxide material belongs to wolframite sub-group [2]. Whitney T. Schaller verified that $CuWO_4{\cdot}xH_2O$ crystals are composed of two water molecules; therefore, it was posteriorly described as copper tungstate dihydrate ($CuWO_4{\cdot}2H_2O$) [1,2]. In general, $CuWO_4{\cdot}2H_2O$ crystals are easily produced by the reaction between copper nitrate and sodium tungstate precursors in aqueous solutions, using specific pH and temperature conditions. Some published papers have reported on the structural features, morphological aspects and electronic properties of this tungstate [3–12]. Particularly, some of these studies [3–7]. consider the $CuWO_4{\cdot}2H_2O$ as a raw or precursor precipitate formed during the initial synthesis stages due to its favorable thermodynamic condition [8–12].

In past years, $CuWO_4$ crystals were obtained by several traditional methods, mainly including oxide mixture or solid state reaction [13–17], flux growth technique [18,19], melting at a high temperature [20], and Czochralski process [21]. Generally, these techniques require high temperatures, long processing times and sophisticated equipment with high maintenance costs [22]. On the other hand, to overcome these drawbacks, simple methods were developed for the preparation of $CuWO_4$ micro- and nanocrystals, such as precipitation reaction [23–26], polyol-mediated at low-temperature [27], hydrothermal conventional [28,29], and microwave-assisted synthesis [30].

* Corresponding author.
E-mail address: laeciosc@bol.com.br (L.S. Cavalcante).

http://dx.doi.org/10.1016/j.ultsonch.2017.03.007
1350-4177/

The wolframite-type monoclinic structure is commonly found in tungstates composed of transition metals belonging to the fourth period of the periodic table ($MnWO_4$ [31], $FeWO_4$ [32], $CoWO_4$ [33], $NiWO_4$ [34], and $ZnWO_4$ [35]). The only exception is $CuWO_4$, which crystallizes in a triclinic structure at room temperature [36–38]. In addition, $CuWO_4$ crystals exhibit a phase transition from triclinic structure at low-pressure to monoclinic structure at high-pressure (9.9 GPa) [39]. Therefore, when subjected to extreme pressure environments, the researchers [40–43] have reported that these crystals have a monoclinic structure characterized by space group ($P2/c$), point group symmetry (C_{2h}^4) and two molecular formula units per unit cell (Z = 2) [43,44]. On the other hand, under low-pressure conditions at room temperature, these crystals exhibit a triclinic structure with space group ($P\bar{1}$), point group symmetry (C_i) and two molecular formula units per unit cell (Z = 2) [45–47]. Moreover, $CuWO_4$ crystals with triclinic structure are influenced by Jahn-Teller effect due to the presence of Cu^{2+} ions, which promote distortions on octahedral [CuO_6] clusters. Consequently, this phenomenon gives rise to a *d*-orbital splitting, in which the degeneracy of σ-antibonding orbitals is broken [48,49]. According to the literature [50,51], the Pauli exclusion principle can provide that the Cu^{2+} ions have an electron with unpaired spin occupying the d_{x-y}^2 orbital, indicating that this electronic level could produce a mid-gap band state. The additional stabilization is greater in a Jahn–Teller-elongated Cu^{2+} ions (where $3d_z^2$ contains two electrons) [52].

Currently, the scientific studies on the electronic properties of pure and doped $CuWO_4$ have been mainly focused on the photocatalytic (PC) degradation of organic dyes (Rhodamine B, eosin yellow dye and methylene blue) under ultraviolet and visible light [53–55], magnetic [56–59], photoelectrochemical water splitting [60–64], visible and solar-assisted water splitting [65,66], photoanode for solar water oxidation [67,68], electrical transport [69], and photoluminescence (PL) [24,53,70]. An important point to be considered is that the theoretical studies [16,71–75], performed by means of *ab initio* calculations based on the density-functional theory (DFT) for the electronic structure of $CuWO_4$ crystals, have shown that the conduction band (CB) of this oxide is composed of 3*d* orbitals (Cu atoms) and 5*d* orbitals (W atoms), while the valence band (VB) is formed of 2*p* orbitals (O atoms).

Therefore, the aim of the present study was to investigate the structural, morphological and optical properties of $CuWO_4$ crystals. These crystals were initially synthesized by the sonochemistry (SC) method (30 min), and then, heat treated in a conventional furnace at different temperatures for 1 h. A crystal growth mechanism was proposed in order to explain the evolution of particle shape/size with the increase of the heat treatment temperature. Finally, the optical properties of these crystals were investigated by Ultraviolet-Visible spectroscopy and PL measurements at room temperature.

2. Experimental details

2.1. Synthesis of $CuWO_4$ crystals

The synthesis of $CuWO_4$ crystals is described as follows: 1×10^{-3} mols of sodium tungstate dihydrate ($Na_2WO_4{\cdot}2H_2O$; 99.5% purity, Sigma-Aldrich) and 1×10^{-3} mols of copper nitrate trihydrate [$Cu(NO_3)_2{\cdot}3H_2O$; 99% purity, Sigma-Aldrich] were separately placed in two plastic tubes (Falcon – capacity of 50 mL) and dissolved with deionized water. The two solutions (pH = 6) were transferred into a beaker (250 mL) and ultrasonicated for 30 min by means of an ultrasonic cleaner (model CPX-1800H, Branson – USA) at frequency of 42 kHz. These suspensions containing bright green precipitates were seven times washed (water and acetone) and centrifuged (8500 rpm for 10 min), and then, dried in a single hot plate (60 °C for 30 min). Finally, the obtained $CuWO_4{\cdot}2H_2O$ precipitates were heat treated at different temperatures (100 °C, 200 °C, 300 °C, 400 °C, and 500 °C for 1 h), maintaining a heating rate of 5 °C.min^{-1}. The increase in the heat treatment temperature was employed to monitor the crystallization process of single $CuWO_4$ phase.

$CuWO_4{\cdot}2H_2O$ crystals were synthesized via chemical reaction between hexaaquacopper(II) complex ion ($[Cu(H_2O)_6]^{2+}$) and tungstate ions (WO_4^{2-}) in aqueous solution. These ions were originated by means of the complete dissolution of their respective chemical precursors [$Na_2WO_4{\cdot}2H_2O$ and $Cu(NO_3)_2{\cdot}3H_2O$], as described in Eqs. (1)--(3):

$$Na_2WO_4 \cdot 2H_2O_{(s)} \xrightarrow{H_2O} 2Na^+_{(aq)} + WO^{2-}_{4(aq)} + 2H_2O \quad (1)$$

$$Cu(NO_3)_2.3H_2O_{(s)} \xrightarrow{H_2O} [Cu(H_2O)_6]^{2+} + 2NO^-_{3(aq)} + 3H_2O \quad (2)$$

$$2Na^+_{(aq)} + WO^{2-}_{4(aq)} + 2H_2O + [Cu(H_2O)_6]^{2+} + 3H_2O \xrightarrow[30]{\text{vv}\ \text{min}} CuWO_4.2H_2O_{(s)} + 2Na^+_{(aq)} + 2NO^-_{3(aq)} + 5H_2O \quad (3)$$

The heat treatment performed at low temperatures (from 100 °C to 200 °C) was responsible for the partial removal of water molecules belonging to $CuWO_4{\cdot}2H_2O$ structure, according to Eq. (4):

$$CuWO_4 \cdot 2H_2O_{(s)} \ldots x.H_2O_{(ads)} \xrightarrow{\approx 100^\circ C \text{and} 200^\circ C/1h} CuWO_4.xH_2O_{(s)} + 2H_2O_{(g)} \quad (4)$$

The water removal (dehydration process) continues at low temperatures (≈300 °C); however, there is a mixture of $CuWO_4{\cdot}xH_2O$ and $CuWO_4$ phases, as proposed in Eq. (5):

$$2CuWO_4 \cdot xH_2O_{(s)} \xrightarrow{\approx 300^\circ C/1h} CuWO_4 \cdot xH_2O_{(s)} + CuWO_{4(s)} \quad (5)$$

The formation of single $CuWO_4$ crystals occurs at temperatures above 400 °C, according to Eq. (6):

$$CuWO_4 \cdot xH_2O_{(s)} + CuWO_{4(s)} \xrightarrow{\approx 400^\circ C \text{and} 500^\circ C/1h} 2CuWO_{4(s)} + xH_2O_{(g)} \quad (6)$$

2.2. Characterizations of $CuWO_4$ crystals

$CuWO_4$ nanocrystals were structurally characterized by X-ray diffraction (XRD) with a DMax/2500PC diffractometer (Rigaku, Japan), using Cu-Kα radiation (λ = 0.15406 nm). Data were collected over 2θ ranging from 10° to 70°, employing a step scan of 2°.min^{-1}. Rietveld analysis was performed over 2θ ranging from 5° to 120°, at a scan step and step size of 1°.min^{-1} and 0.02°, respectively. Thermogravimetric analysis (TGA) and differential thermal analysis (DTA) were carried out in a STA 409 thermal analyzer (Netzsch, Germany). These thermal measurements were performed from room temperature to 550 °C under synthetic air flow (15 cm^3.min^{-1}), maintaining a heating rate of 10 °C.min^{-1}. Micro Raman (M-Raman) spectra were recorded using a LabRAM HR 800 spectrometer (Horiba Jobin Yvon, France). These spectra were

obtained from 50 cm^{-1} to 1000 cm^{-1} with an Ar^{+} laser of 514.5 nm (model CCD DU420AOE325), maintaining a maximum output power of 6 mW. A 50 μm lens was used to prevent sample overheating. Fourier Transform infrared (FT-IR) spectra were performed from 200 cm^{-1} to 1000 cm^{-1} with a Bomem–Michelson spectrophotometer operated in transmittance mode (model MB-102). Ultraviolet–Visible (UV–Vis) spectra were taken using a Cary 5G spectrophotometer (Varian, USA) operated in diffuse reflectance mode. The morphological features were examined by using a Supra 35-VP field-emission scanning electron microscope (FE-SEM) (Carl Zeiss, Germany) operated at 10 kV, and with a CM200 transmission electron microscope (TEM) (Philips/FEI, Netherlands) operated at 200 kV. The shape, average size and crystal growth directions of $CuWO_4$ crystals were determined using the selected-area electron diffraction (SAED) and high resolution (HR)-TEM, respectively. The samples for TEM and HR-TEM were prepared depositing (dropwise) dilute suspensions of $CuWO_4$ crystals in acetone on 300-mesh Cu grids. The photoluminescence (PL) spectra were conducted at room temperature by using a Monospec 27 monochromator (Thermal Jarrel Ash, USA) coupled to a R955 photomultiplier (Hamamatsu Photonics, Japan). A krypton-ion laser (Coherent Innova 90 K; λ = 350 nm) was used as an excitation source, maintaining a maximum output power at 500 mW. The laser beam passed through an optical chopper, so that the maximum power incident on the sample was maintained at 14 mW.

3. Results and discussions

3.1. Long-range structural analyses

Fig. 1(a, b) shows XRD patterns of $CuWO_4{\cdot}2H_2O$ and $CuWO_4$ crystals heat treated at different temperatures, respectively.

According to the literature [76], the degree of structural order/disorder or periodicity of a crystalline lattice in oxide materials can be analyzed by means of X-ray diffraction. In Fig. 1(a), the precipitated crystals heat treated at 100 °C and 200 °C for 1 h revealed the presence of wide XRD peaks assigned to $CuWO_4{\cdot}2H_2O$ monoclinic structure. This widening can be due to the presence of water molecules bonded in this crystalline structure (TGA and DTA profiles in Support Information Fig. SI-1(a, b)) as well as because of effects of order–disorder [77], i.e., these crystals have not a complete long-range structural ordering. Increasing the heat treatment temperature up to 300 °C (Fig. 1(a)), XRD patterns revealed a mixture of $CuWO_4{\cdot}2H_2O$ and $CuWO_4$ phases. Therefore, in this temperature occurs a significant elimination of water molecules in $CuWO_4{\cdot}2H_2O$. Chen and Xu [28] described the $CuWO_4{\cdot}2H_2O$ crystals as a crystalline phase with monoclinic structure referring to JCPDS Card Nº. 33-0503. When the heat treatment was performed at 400 °C and 500 °C for 1 h, all XRD patterns showed diffraction peaks ascribed to $CuWO_4$ triclinic structure, in agreement with the ICSD card Nº. 16009 [78]. In order to confirm this triclinic structure, the structural refinement by means of Rietveld method [79] was performed for $CuWO_4$ crystals heat treated at 500 °C for 1 h.

The Rietveld method is based on the construction of diffraction patterns calculated according to a structural model [80]. The calculated patterns are adjusted to the observed pattern, providing the structural parameters of the desired material and its diffraction profile. In the present study, the Rietveld method was applied to estimate the atomic positions, lattice parameters, and unit cell volume of $CuWO_4$ crystals. The Rietveld refinement was performed using the general structure analysis software (GSAS) program [81], in which the refined parameters were scale factor, background, shift lattice constants, profile half-width parameters (*u*, *v*, *w*), isotropic thermal parameters, lattice parameters, strain anisotropy factor, preferential orientation, factor occupancy, and atomic functional positions. The background was corrected using a Chebyschev polynomial of the first order. The peak profile function was modeled using a convolution of the Thompson–Cox–Hastings pseudo-Voigt (pV-TCH) function [82] with the asymmetry function described by Finger et al. [83] In order to explain the anisotropy in the half width of the reflections, the model by Stephens [84] was used.

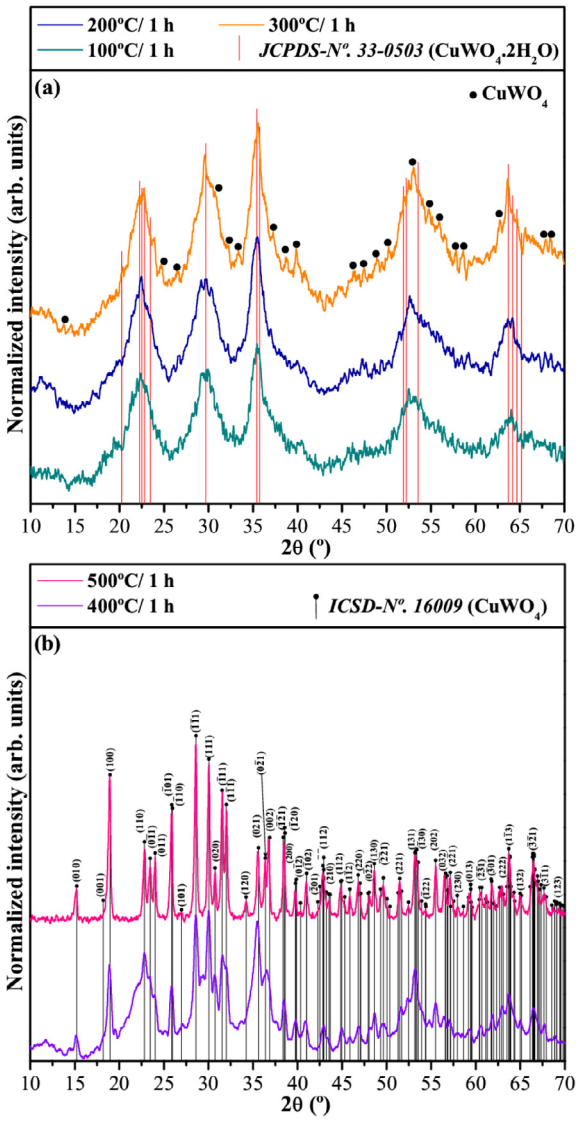

Fig. 1. XRD patterns of (a) $CuWO_4{\cdot}2H_2O$ and (b) $CuWO_4$ crystals, respectively. The vertical lines in red color indicate the position and relative intensity of XRD patterns for $CuWO_4{\cdot}2H_2O$ phase reported in Joint Committee on Powder Diffraction Standards (JCPDS) card Nº. 33-0503. The symbol (•) is assigned to $CuWO_4$ phase. The vertical lines in black color show the position and relative intensity of XRD patterns for $CuWO_4$ phase described in Inorganic Crystal Structure Database (ICSD) card Nº. 16009.

Fig. 2 shows the Rietveld refinement plot for $CuWO_4$ crystals synthesized by the SC method and heat treated at 500 °C for 1 h.

All structural refinement results obtained by the Rietveld method [80] are consistent with ICSD Nº. 16009 reported by Kihlborg and Gebert [78]. According to the literature [85], single $CuWO_4$ crystals have a triclinic structure, presenting a space group ($P\bar{1}$), point group symmetry (C_i) and two molecular formula units per unit cell (Z = 2). The structural refinement confirmed the triclinic structure for $CuWO_4$ crystals (Fig. 2). In general, slight

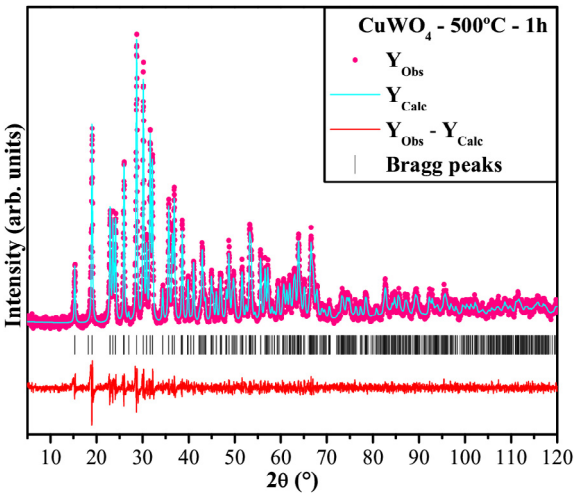

Fig. 2. Rietveld refinement plot of $CuWO_4$ crystals heat treated at 500 °C for 1 h.

differences in the intensity scale were identified between experimental and calculated XRD patterns, as described by the line (Y_{Obs}–Y_{Calc}). However, the quality of the structural refinement can be accurately determined by the *R*-values (R_{wp}, R_{Bragg}, R_p, χ^2, and *S*). More details on the Rietveld refinement results are displayed in Table 1.

In this table, the fit parameters (R_{Bragg}, R_{wp}, R_p, χ^2, and *S*) suggest that refinement results are very reliable. In general, small variations in atomic positions of O atoms were identified, while Cu and W atoms are fixed in their respective positions within the structure. In this case, the O atoms are able to induce distortions on both O–Cu–O or O–W–O bonds, resulting in distorted octahedral [CuO_6] and [WO_6] clusters.

3.2. Structural representation, and coordination of clusters in $CuWO_4$

Fig. 3 shows a schematic representation of $CuWO_4$ triclinic structure.

This triclinic structure was modeled through the visualization system for electronic and structural analysis (VESTA) software (version 3.4.0 for version of Windows 7-64-bit) [86,87], using the lattice parameters and atomic positions obtained from the Rietveld refinement data listed in Table 1. In Fig. 3, Cu and W atoms are both coordinated to six O atoms, forming distorted octahedral [CuO_6] and [WO_6] clusters, which are octahedron-type polyhedrons with 6-vertices, 8-faces and 12-edges [88]. In principle, these $CuWO_4$ crystals heat treated at different temperatures are able to present variations in both (O–Cu–O)/(O–W–O) bond angles and lengths. This behavior implies in distortions on octahedral [CuO_6] and [WO_6] clusters with distinct degrees of order–disorder in the lattice.

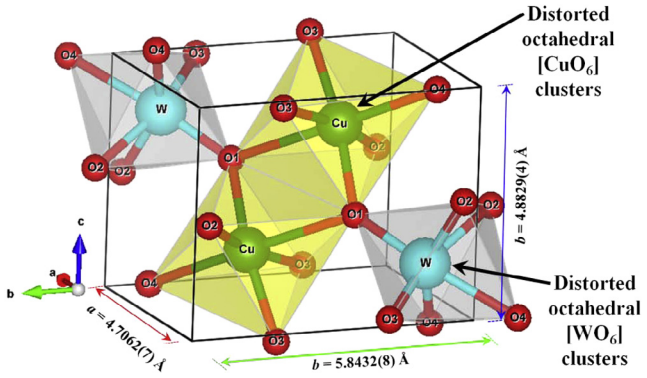

Fig. 3. Schematic representation of $CuWO_4$ triclinic structure.

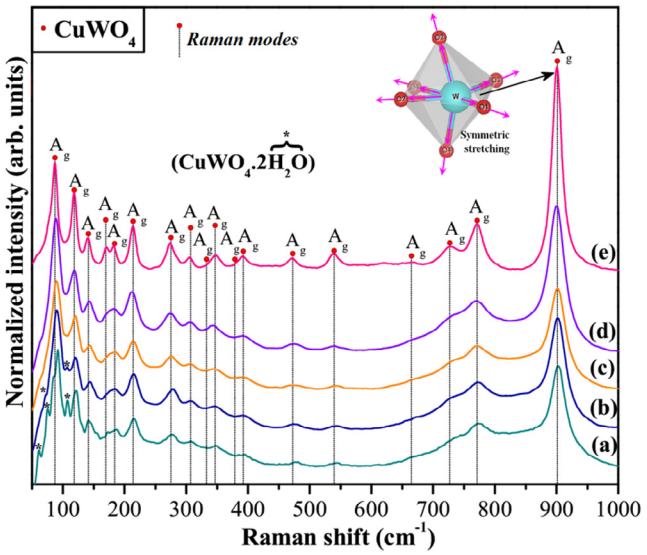

Fig. 4. Micro-Raman spectra of $CuWO_4$ crystals heat treated at (a) 100 °C, (b) 200 °C, (c) 300 °C, (d) 400 °C and (e) 500 °C for 1 h. Inset shows a typical symmetric stretching vibration of O–W–O bonds in octahedral [WO_6] clusters. The vertical dotted lines with symbol (●) indicate the relative positions and intensities of Raman-active modes of $CuWO_4$ crystals, while the symbol (*) show the presence of water molecules within these crystals, respectively.

3.3. Short-range structural analysis

Fig. 4(a–e) shows the M-Raman spectra of $CuWO_4$ crystals heat treated at different temperatures.

The short-range structural ordering in the lattice of any material can be analyzed via Raman spectroscopy [89]. According to group theory calculations, tungstates with triclinic structure, space group ($P\bar{1}$) and point group symmetry (C_i) have 36 different

Table 1
Rietveld refinement results for $CuWO_4$ crystals obtained by the sonochemistry method and heat treated at 500 °C for 1 h.

Atoms	Wyckoff	Site	x	y	z
Cu	2*i*	1	0.4959(5)	0.6589(9)	0.2450(6)
W	2*i*	1	0.0202(8)	0.1729(2)	0.2538(3)
O1	2*i*	1	0.2472(9)	0.3569(4)	0.4257(0)
O2	2*i*	1	0.2126(9)	0.8846(4)	0.4321(0)
O3	2*i*	1	0.7334(9)	0.3837(4)	0.0993(0)
O4	2*i*	1	0.7334(9)	0.9131(4)	0.0545(0)

a = 4.7062(7) Å, *b* = 5.8432(8) Å, *c* = 4.8829(4) Å, α = 91.6680(3)°, β = 92.4985(3)°, γ = 82.7871(3)°; V = 133.054(7)Å^3, R_{Bragg} (%) = 2.50, R_{wp} (%) = 8.84, R_p (%) = 6.89, χ^2 = 1.17 and *S* = 1.08166.

{(Raman) and [infrared]} vibrational modes, as described in Eq. (7) [40,41,71].

$$\Gamma_{\{(\text{Raman})+[\text{Infrared}]\}} = \{(18A_g) + [18A_u]\} \quad (7)$$

where A_g are Raman-active vibrational modes, and A_u are infrared-active vibrational modes. Therefore, 18 Raman-active vibrational modes are expected for $CuWO_4$ crystal, shown in Eq. (8):

$$\Gamma_{(\text{Raman})} = 18A_g \quad (8)$$

According to the literature [71,90], vibrational modes observed in Raman spectra of tungstates are classified into two groups, external and internal modes. The vibrational external modes are related to lattice phonons, corresponding to the motion of distorted octahedral [CuO_6] clusters (O_h symmetry) and rigid units. Vibrational internal modes are ascribed to vibrations of distorted octahedral [WO_6] clusters in the lattice, assuming the center of mass in a stationary state. Distorted octahedral [WO_6] clusters have point group symmetry (C_i), in which the vibrations are composed of internal modes (A_g); the other vibrations are external modes (A_g) [91]. As can be observed in Fig. 4(a–e), there are Raman-active modes for the two crystals ($CuWO_4.2H_2O$ and $CuWO_4$). Firstly, the samples heat treated at 100 °C and 200 °C have vibrational modes arising from water molecules ($_*H_2O$) in $CuWO_4.2H_2O$ crystals (Fig. 4(a, b)). The disappearing or lower intensity of these Raman-active modes in the spectrum illustrated in Fig. 4(c) indicates that the temperature of 300 °C is critical for a phase transition from $CuWO_4{\cdot}2H_2O$ (monoclinic structure) to $CuWO_4$ crystals (triclinic structure). In Fig. 4(d, e), when the samples were heat treated at 400 °C and 500 °C for 1 h, the Raman-active vibrational modes are only ascribed to $CuWO_4$ triclinic structure. Another important point to be considered is that the heat treatment at 500 °C resulted in more intense and well-defined Raman-active bands for $CuWO_4$ crystals. In this case, the evolution of temperature also leads to an increase of short-range structural ordering for this oxide. Table 2 shows a comparative between the respective positions of Raman-active vibrational modes for $CuWO_4$ reported experimentally and theoretically in papers published in the literature [41] with those obtained in our present study.

In this table, there is a good agreement between our experimental Raman-active vibrational modes with the reported in other papers previosly published [40–42,92]. The slight displacements in the positions of these vibratiol modes can be related to variations in the degree of structural order-disorder on both octahedral [CuO_6] and [WO_6] clusters, as a consequence of the peculiarities of each synthesis condition (temperature, time) adopted for the formation of $CuWO_4$ phase.

3.4. FT-IR spectroscopy analyses

Fig. 5(a–e) illustrate FT-IR spectra of $CuWO_4$ crystals heat treated at different temperatures.

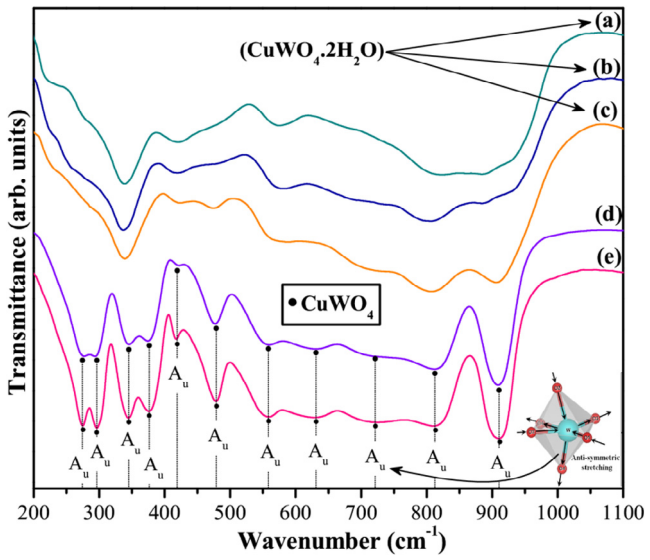

Fig. 5. FT-IR spectra of $CuWO_4$ crystals heat treated at (a) 100 °C, (b) 200 °C, (c) 300 °C, (d) 400 °C and (e) 500 °C for 1 h. Inset shows a typical anti-symmetric stretching vibration of O–W–O bonds in octahedral [WO_6] clusters. The vertical dotted lines with symbol (•) indicate the relative positions and intensities of IR-active modes.

Table 2
Comparative data of the respective positions of Raman-active modes of $CuWO_4$ reported in the literature with those obtained in the present study.

	M	–	THEO	TSSG	SC-C	SC-C	SC-C
	T (°C)	–	–	1000	500	400	500
	t (h)	–	–	48	5	1	1
R	A_{1g}	95.3	81	–	–	87.4	86.8
a	A_{1g}	127.6	115.6	–	–	118.2	118.3
m	A_{1g}	149.1	137.7	–	–	140.1	140.2
a	A_{1g}	179.2	164.4	180	–	170.2	170.2
n	A_{1g}	191	178	192	190	181.1	181.2
	A_{1g}	223.8	209.2	224	223	213.1	213.4
A	A_{1g}	282.6	263.5	283	279	272.2	272.4
c	A_{1g}	292.6	276.2	293	314	304.8	305.5
t	A_{1g}	316.2	294.3	315	395	331.2	332
i	A_{1g}	358.2	341	358	447	346.8	347.2
v	A_{1g}	397.5	374.9	398	547	380.3	381.2
e	A_{1g}	403.4	391.9	405	447	392.8	391.2
	A_{1g}	479.9	454.1	479	547	472.1.	472.3
M	A_{1g}	549.8	525.2	550	673	538.1	538.8
o	A_{1g}	676.7	633.6	676	731	665.7	667.6
d	A_{1g}	733.1	695.8	733	778	728.8	729.1
e	A_{1g}	778.9	763.2	779	805	769.1	771.5
s	A_{1g}	905.9	854.4	906	905	900.9	901.2
	Ref.	[40]	[41]	[42]	[92]	✠	✠

M = Method; *t* = time; Raman modes = (cm^{-1}); THEO = Theoretical, TSSG = top-seeded solution growth; SC-C = Sonochemical-Calcination; [✠] = This work and Ref. = References.

According to the literature [93], IR spectra also is able to provide information on the degree of structural order-disorder in atomic bonds of ABO_4 materials. Eq. (7) shows that the $CuWO_4$ crystals with triclinic structure have 18 Raman-active vibrational modes and 18 IR-active vibrational modes, as indicated by Eq. (9) [94]:

$$\Gamma_{[\text{Infrared}]} = 18A_u \quad (9)$$

As illustrated in Fig. 5(a–e), only eleven IR-active vibrational bands [A_u modes] were detected in our IR spectra. This behavior is explained by the low symmetry of $CuWO_4$ lattice and phonon pattern associated with each mode that is in general complex and involves the whole unit cell [94]. However, the atom dynamics associated to highest energy modes can be understood on the basis of the main atomic shifts [94,95]. The band located at around 910 cm^{-1} is related to symmetric stretching vibrations (←O←W→O→) in distorted octahedral [WO_6] clusters. It was noted a smaller band at 812 cm^{-1}, which cannot be related to optical modes at zone center [94]. Another band of low intensity at 720 cm^{-1} is related to anti-symmetric stretching vibrations in distorted octahedral [WO_6] clusters (Inset Fig. 5). Also, it was noted a shoulder at 631 cm^{-1} [A_u mode], which cannot be attributed to optical modes [94]. The symmetric stretching vibrations (←O←W→O←W→O→) between [WO_6]–[WO_6] clusters were verified at 558 cm^{-1}. On the other hand, the symmetric stretching vibrations (←O←Cu→O→) of distorted octahedral [CuO_6] clusters were detected at 478 cm^{-1}. The small band at 417 cm^{-1} is arising from symmetric bending vibrations (↖O↖W↗O↗) in [WO_6] clusters.[94] Finally, the last four modes (from 275 cm^{-1} to 377 cm^{-1}) are assigned to anti-symmetric (→O→Cu→O↖Cu↖O↖) and symmetric (←O←Cu→O←Cu→O→) stretching vibrations between [CuO_6]–[CuO_6] clusters, and symmetric bending vibrations (↖O↖Cu↗O↗) in [CuO_6] clusters, respectively. A comparison between the respective positions of IR-active vibrational modes of $CuWO_4$ obtained in our study with others published in the literature [41] are listed in Table 3. As expected in this table, our experimental IR-active vibrational modes are in good agreement with the results verified in other papers [41,94–97]. In addition, we have noted that some of these infrared vibrational modes of $CuWO_4$ nanocrystals are similar to isostructural $CuMoO_4$ crystals [98].

3.5. FE-SEM images analyses

Fig. 6(a–e) shows FE-SEM images of $CuWO_4$ crystals heat treated at different temperatures.

FE-SEM micrographs can be used as a powerful tool to accompany the particle shape evolution and growth process of $CuWO_4$ nanocrystals. Fig. 6(a) shows that the $CuWO_4{\cdot}2H_2O$ microcrystals obtained at 100 °C have a similar aspect of irregular flowers, which are formed by aggregated assemblies of several crystals (as "petals"). These "petals" show many imperfections and surface defects, as a direct result of both uncontrollable formation and interaction of nanocrystals caused by the chemical synthesis employed, solvent nature or intrinsic morphological feature of $CuWO_4{\cdot}2H_2O$ microcrystals [64]. These final structures similar to flowers have an average size of 4.7 μm, while their petals have an average size of 860 nm (Support Information Fig. SI-2(a, b)). When the heat treatment was performed at 200 °C, both shape and size of these crystals were modified. This morphological change can be due to the initial stage of elimination of water molecules in $CuWO_4{\cdot}2H_2O$, resulting in irregular stone-like microcrystals with average crystal size of 3.3 μm (Fig. 6(b)). These microcrystals are composed of several aggregated nanocrystals with average size of approximately 7.7 nm (Support Information Fig. SI-2(c, d)). In Fig. 6(c), the increase of heat treatment temperature up to 300 °C was able to maintain the morphological feature of stone-like microcrystals in the samples. In this case, it was estimated for these microcrystals an average size of approximately 6.6 μm, in which their aggregated nanocrystals presented an average crystal size of 11 nm (Support Information Fig. SI-2(e, f)). In Fig. 6(d), the presence of a large number of small crystals was verified on the surface of stone-like microcrystals heat treated at 400 °C for 1 h. As detected by XRD patterns (Fig. 1(b)), in this temperature occurs only the presence of $CuWO_4$ triclinic structure. Therefore, the counting of these stone-like $CuWO_4$ microcrystals revealed an average size at around 9.3 μm, which are formation by irregular nanocrystals with average size of 18.3 nm (Support Information Fig. SI-2(g, h)). Finally, for the temperature of 500 °C, it was possible to prove that these large stone-like microcrystals are composed of several flake-like $CuWO_4$ nanocrystals. For these

Table 3
Comparative data of the respective positions of IR-active modes of $CuWO_4$ reported in the literature with those obtained in the present study.

	M	THEO	TSSG	CP-C	CP-C	SSR	SC-C	SC-C
	T (°C)	–	1000	450	800	800	400	500
	t (h)	–	48	6	8	36	1	1
I	A_{1u}	–	–	–	–	–	–	–
n	A_{1u}	–	–	–	–	–	–	–
f	A_{1u}	–	–	–	–	–	–	–
r	A_{1u}	101.4	–	–	–	–	–	–
a	A_{1u}	157.3	–	–	–	–	–	–
r	A_{1u}	214.2	–	–	–	–	–	–
e	A_{1u}	239	253	–	–	–	–	–
d	A_{1u}	266.1	275	–	–	270	274	275
	A_{1u}	281	290	–	–	290	296	297
Ac	A_{1u}	320.5	355	–	–	340	344	345
ti	A_{1u}	332.3	–	–	–	375	376	377
ve	A_{1u}	383.8	395	–	–	415	416	417
	A_{1u}	438.9	466	500	–	–	477	478
M	A_{1u}	474.8	540	–	545	550	557	558
o	A_{1u}	516.5	600	–	–	605	630	631
d	A_{1u}	639.6	722	–	710	740	719	720
e	A_{1u}	727.7	760	748	799	800	811	812
s	A_{1u}	852.7	911	876	900	910	909	910
	Ref.	[40]	[94]	[95]	[96]	[97]	✠	✠

M = method; T = temperature; *t* = time; IR-active modes = (cm^{-1}); TSSG = Top-seeded solution growth; CP-C = Co-precipitation-Calcination; SSR = Solid state reaction; SC-C = Sonochemical-Calcination; THEO = Theoretical, and [✠] = this work.

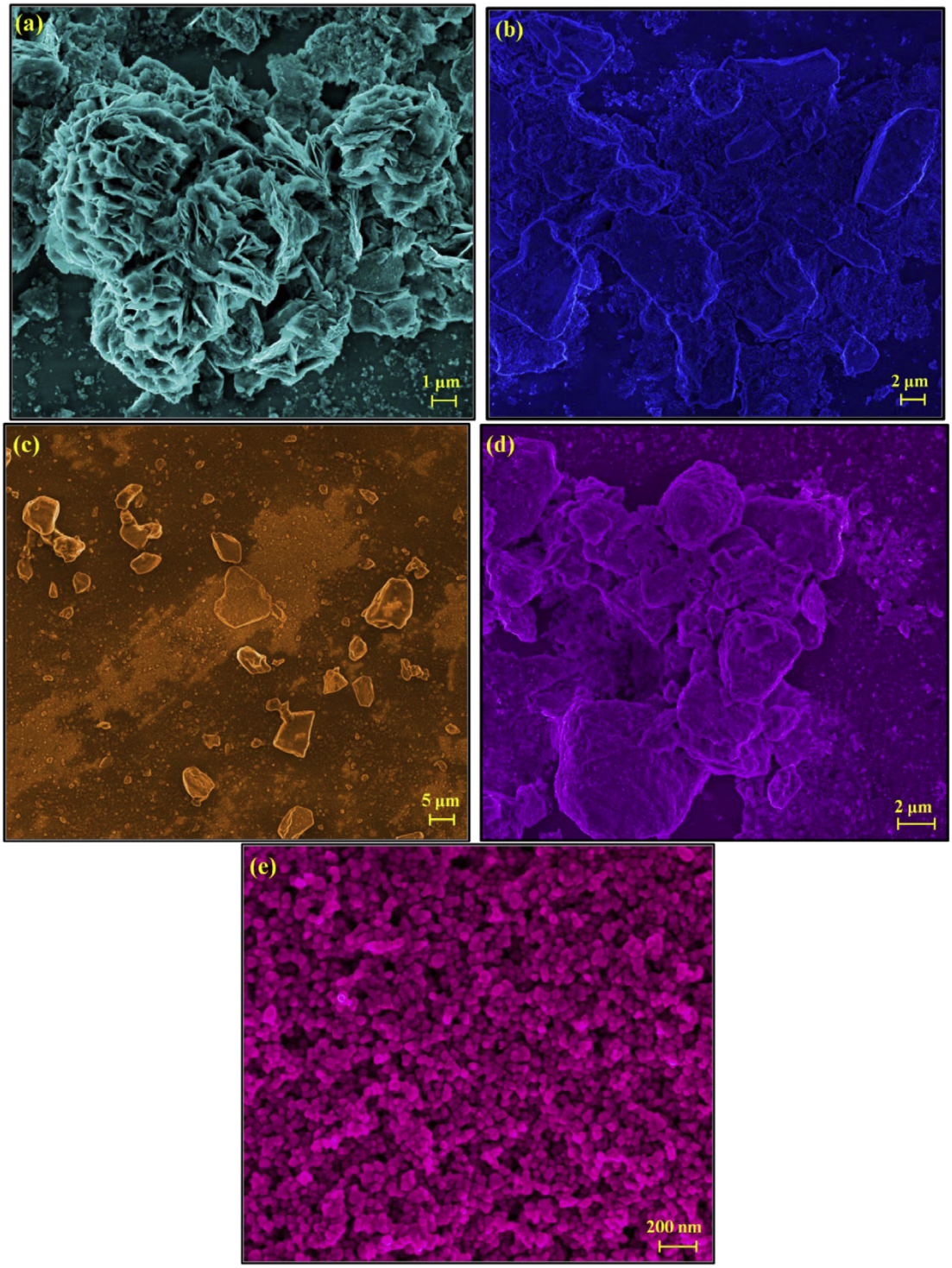

Fig. 6. FE-SEM images of $CuWO_4$ crystals heat treated at different temperatures: (a) 100 °C, (b) 200 °C, (c) 300 °C, (d) 400 °C and (e) 500 °C for 1 h, respectively.

nanocrystals was found an average size of approximately 41 nm (Support Information Fig. SI-2(i)). All results on the average size distribution of $CuWO_4$ crystals are summarized in Table 4 and (Support Information Fig. SI-2(a–i)).

All experimental results obtained in our study are good agreement with the literature [99–103]. In addition, all statistical data obtained through the counting of particle sizes using FESEM and TEM images were well-described by the log-normal distribution [104].

3.6. TEM and HR-TEM images analyses

Fig. 7(a–j) show TEM and HR-TEM images of $CuWO_4$ crystals heat treated at different temperatures.

Based on the TEM characterization for the material obtained at 100 °C, it was possible to confirm that the "petals" are originated by the joint between several nanocrystals, which are able to aggregate to form the flower-like microcrystals. Fig. 7(a) shows the presence of some nanoparticles attached in a common crystallographic

Table 4
Comparative results between the morphological features (crystal size and shape) and optical band gap energy (E_{gap}) of $CuWO_4$ crystals heat treated at different temperatures for 1 h obtained in the present study with those reported in the literature.

M	Crystal shape	Average crystal size (nm)*/(μm) ■	T(°C)	t(h)	E_{gap} (eV)	Ref.
HC	Hollow microspheres	300*	180	18	2.3	[99]
SC-C	Nanoparticles	30–50*	500	2	3.2	[100]
HC/CC	Nanoflakes	30*/1■	450	1	2.22	[101]
MI-C	Nanoparticles	31.8*	500	2	–	[102]
P-C	Nanoparticles	50*	500	1	2.0	[103]
SC-C	Petal-like/Flower-like	860*/4.68■	100	1	2.45	✠
SC-C	Flakes-like/Rough stones-like	7.664*/3.32■	200	1	2.28	✠
SC-C	Flakes-like/Rough stones-like	11*/6.653■	300	1	2.34	✠
SC-C	Flakes-like/Rough stones-like	18.3*/9.313■	400	1	2.24	✠
SC-C	Flakes-like	41*	500	1	2.19	✠

M = method; T = temperature; *t* = time; HC = Hydrothermal conventional; SC-C = Sonochemistry-Calcination; CC = Chemical conversion; MI-C = Microwave irradiation-Calcination; P-C = Polyol-Calcination; [✠] = This work.

orientation. HR-TEM image presented in Fig. 7(b) shows the presence of nanocrystals with diameters of approximately 4 nm. The interplanar distance for these nanocrystals was estimated in approximately 0.23 nm, which correspond to (200) crystallographic plane of $CuWO_4$ triclinic phase, which is present in small points locally in the hydrated global lattice. The selected area electron diffraction (SAED) image (inset in Fig. 7(b)) was indexed also as $CuWO_4$ phase. In this case, it is important to emphasize that both TEM and SAED focused on some nanocrystals locally indicate the $CuWO_4$ phase, while X-ray patterns, due to be a long-range technique, indicated the $CuWO_4{\cdot}2H_2O$ phase. The low resolution TEM image for the sample obtained at 200 °C showed several aggregated nanoparticles (Fig. 7(c)). SAED (not shown here) indicated the presence of low intensity rings related to nanocrystalline particles, which is supported by HR-TEM image in Fig. 7(d). The materials heat treated at 300 °C are illustrated in Fig. 7(e, f). Again, the micrographs revealed that the stone-like $CuWO_4$ microcrystals are clearly formed by randomly distributed aggregated nanoparticles, as confirmed by low intensity rings in SAED (Inset in Fig. 7(f)). HR-TEM image also revealed the same interplanar distance (0.23 nm), as observed in Fig. 7(b), i.e., proving the $CuWO_4$ triclinic phase. Exactly, this same behavior was also identified for the materials obtained at 400 °C (Fig. 7(g, h)). For the material heat treated at 500 °C, the existence of larger particles was identified, in which some of them are well-faceted (high degree of crystallinity). TEM images also showed these particles are agglomerated instead of aggregated, presenting an interplanar distance of 0.31 nm related to $(\bar{1}\bar{1}1)$ plane of $CuWO_4$ triclinic phase. The other TEM and HR-TEM images can support the explanations above as found in Support Information Figs. SI-3(a–j). All experimental results obtained in this study are in good agreement with the literature and presented in Table 4 [99–103]. Therefore, TEM images provides some advantages over SEM images, specially confirming that larger particles for samples obtained from 200 °C to 400 °C are composed of smaller nanoparticles. On the other hand, the particles observed at 500 °C are single-crystalline. SAED agrees with XRD results, in which the synthesis method allowed the formation of crystalline nanoparticles of $CuWO_4$.

3.7. Crystal growth mechanism

Fig. 8(a–k) shows a schematic representation of all stages involved in the synthesis and growth of $CuWO_4$ nanocrystals synthesized by the SC method and heat treated at different temperatures for 1 h.

Initially, there is the coulomb interaction between $[Cu(H_2O)_6]^{2+}$ and WO_4^{2-} complex ions in aqueous solution, promoting the formation of first $CuWO_4{\cdot}2H_2O$ nuclei (Fig. 8(a, b)). These nuclei control the kinetics of nucleation and growth of $CuWO_4$ nanocrystals. In the next growth stage (Fig. 8(c, d)), the crystals in the aqueous medium are able to rotate and align to find a common crystallographic plane via self-assembly process. As this process is uncontrollable, there is the random and spontaneous aggregation of nanocrystals, resulting in petal-like $CuWO_4{\cdot}2H_2O$ microcrystals (Fig. 8(e)). After heat treatment performed at 100 °C for 1 h, flower-like $CuWO_4{\cdot}2H_2O$ microcrystals are formed, which are composed of several petal-like crystals (Fig. 8(f)). The initial stage of elimination of water molecules in $CuWO_4{\cdot}2H_2O$ due to the heat treatment temperature at 200 °C resulted in irregular stone-like microcrystals (Fig. 8(g)). The progressive removal of these water molecules in the lattice with the increase of heat treatment promoted a phase transition from $CuWO_4{\cdot}xH_2O$ (monoclinic structure) to $CuWO_4$ crystals (triclinic structure). However, for temperatures of 300 °C and 400 °C, the morphological aspect of irregular stone-like microcrystals is maintained (Fig. 8(i, j)). Finally, when the materials were heat treated at 500 °C, $CuWO_4$ crystals grew by means of nanocrystals. These results can be proved through FESEM, TEM and HR-TEM images (Figs. 6(e) and 7(i, j)).

3.8. Uv–vis spectra and optical band gap energy

The optical band gap energy (E_{gap}) was calculated using the method proposed by Kubelka and Munk [105]. This methodology is based on the transformation of diffuse reflectance measurements to estimate E_{gap} values of semiconductors with good accuracy [106]. The Kubelka–Munk Eq. (10) for any wavelength is defined as:

$$F(R_\infty) \equiv \frac{(1-R_\infty)}{2R_\infty} = \frac{k}{s} \tag{10}$$

where $F(R_\infty)$ is the Kubelka–Munk function or absolute reflectance of the sample. In our case, magnesium oxide (MgO) was adopted as standard in reflectance measurements. $R_\infty = R_{sample}/R_{MgO}$, where R_∞ is the reflectance, k is the molar absorption coefficient, and s is the scattering coefficient. The optical band gap and absorption coefficient of semiconductor oxides [107] can be calculated using the following Eq. (11):

$$\alpha h\nu = C_1(h\nu - E_{gap})^n \tag{11}$$

where α is the linear absorption coefficient of the material, $h\nu$ is the photon energy, C_1 is a proportionality constant, and n is a constant associated to the type of electronic transition (n = 0.5, 2, 1.5, and 3 for direct allowed, indirect allowed, direct forbidden, and indirect forbidden transitions, respectively). According to Lalic et al. [72] and Lacomba-Perale et al. [108] $CuWO_4$ crystals have an optical absorption spectrum governed by indirect electronic transitions

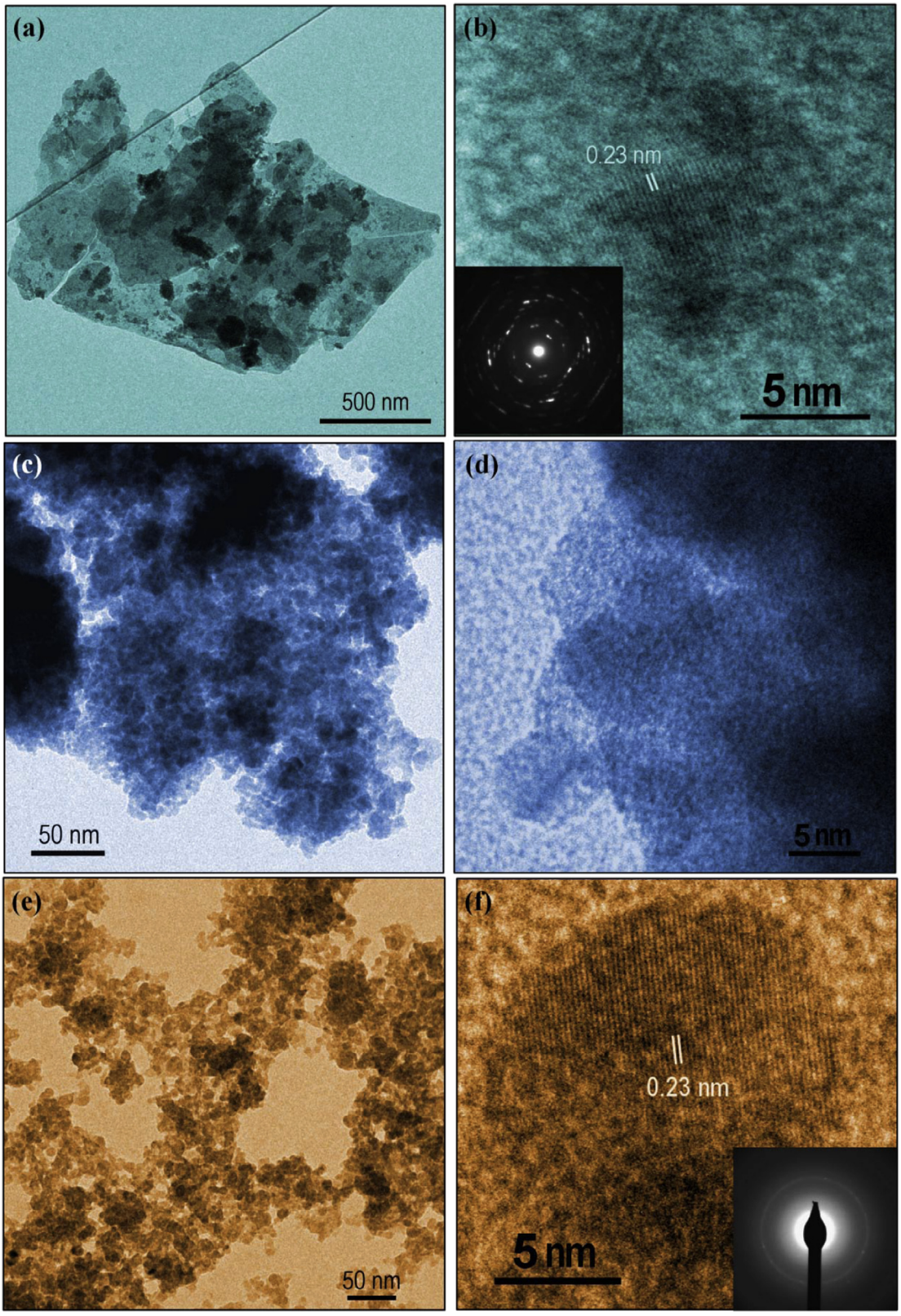

Fig. 7. TEM/HR-TEM images and SAED of $CuWO_4$ crystals heat treated at different temperatures: (a, b) 100 °C, (c, d) 200 °C, (e, f) 300 °C, (g, h) 400 °C and (i, j) 500 °C for 1 h, respectively.

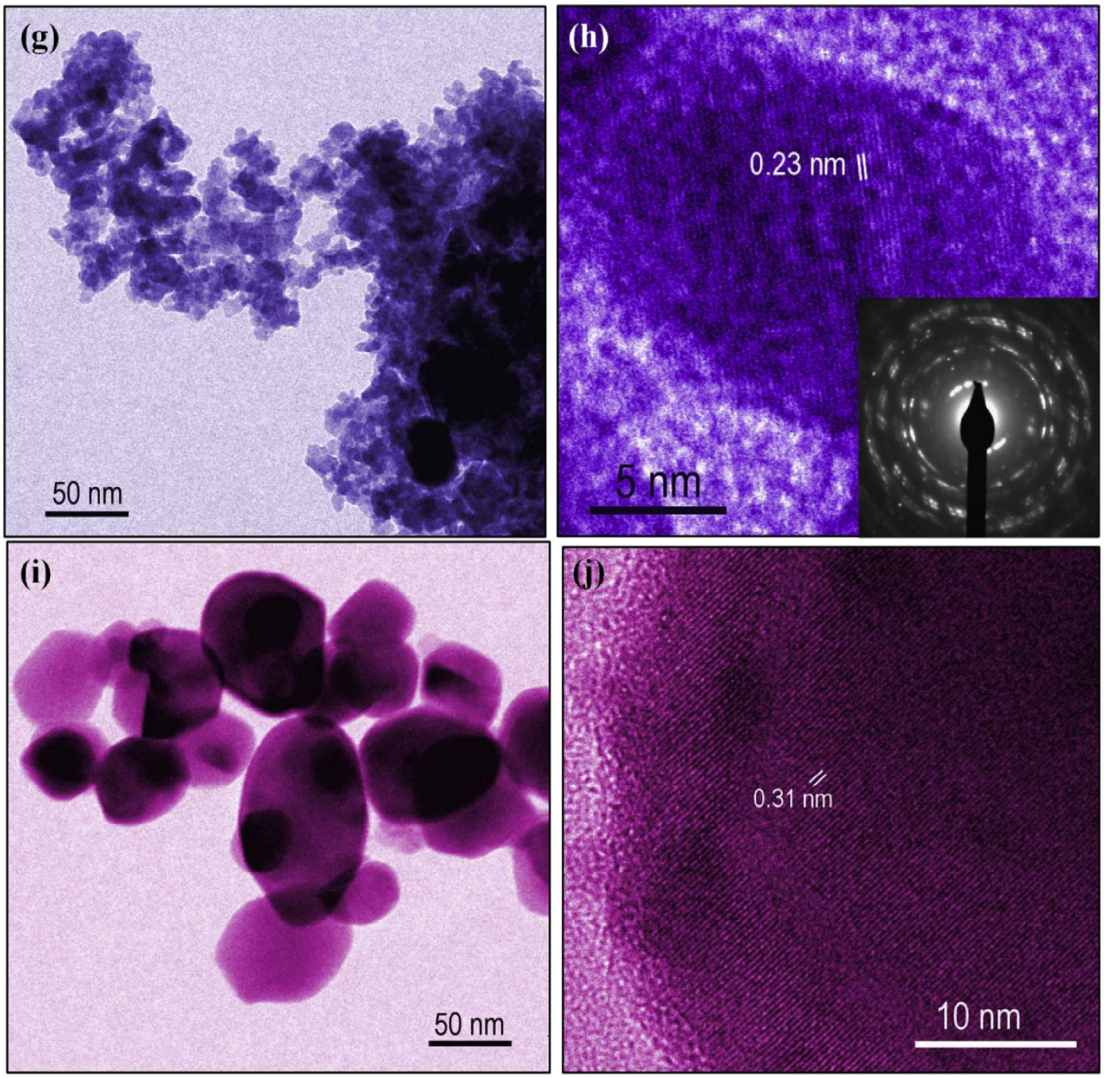

Fig. 7 (*continued*)

between the valence band (VB) and conduction band (CB). After the electronic absorption process, the electrons located in the maximum-energy states in VB return indirectly to minimum-energy states in CB (different points in the Brillouin zone) [109]. Based on this information, E_{gap} values of $CuWO_4$ crystals were calculated using $n = 2$ in Eq. (11). Finally, using the remission function described in Eq. (10) with the term $k = 2\alpha$ and C_2 as a proportionality constant, the modified Kubelka–Munk equation can be obtained, as indicated by Eq. (12):

$$[F(R_\infty)hv]^{\frac{1}{2}} = C_2(hv - E_{gap}) \quad (12)$$

By finding the $F(R_\infty)$ value from Eq. (12) and plotting $[F(R_\infty)hv]^{1/2}$ against hv, the E_{gap} value of $CuWO_4$ crystals was determined.

Fig. 9(a–f) shows the UV–vis diffuse reflectance spectra of $CuWO_4$ crystals heat treated at (a) 100 °C, (b) 200 °C, (c) 300 °C, (d) 400 °C, and (e) 500 °C for 1 h, (f) optical band gap values as a function of temperature.

In this figure, a slight decrease in E_{gap} values with the increase in the heat treatment temperature was detected. This behavior, for samples heat treated from 100 °C to 300 °C, is related to remotion of water molecules (dehydration process) in the lattice, resulting in a phase transition from $CuWO_4{\cdot}xH_2O$ to $CuWO_4$, modifying the number and organization of intermediary energy levels between the VB and CB (Fig. 9(a–c)). Moreover, the exponential optical absorption profile as well as E_{gap} are controlled by the degree of structural order-disorder in the lattice [110]. For samples heat treated at 400 °C and 500 °C, there is only single $CuWO_4$ triclinic phase; therefore, the decrease in E_{gap} values (2.24 and 2.19 eV) can be explained by the presence of low symmetry and distortions on both octahedral [CuO_6] and [WO_6] clusters in the lattice. However, the contributions of electronic levels in these crystals can be achieved only by means of theoretical calculations, which will be perforated in a future study.

3.9. Photoluminescence properties

Fig. 10(a–e) illustrates PL spectra at room temperature of $CuWO_4$ crystals heat treated at different temperatures.

In the last years, the experimental results previosly reported in the literature [26,53,70] have explained the key factors or variables responsible for PL properties of $CuWO_4$ crystals. Pourmortazavi et al. [26,70] and, ReddyPrasad and Naidoo [53] described the PL emission of these crystals with the electronic transitions within complex structure of WO_4^{2-} anion molecular as well as by the trap-

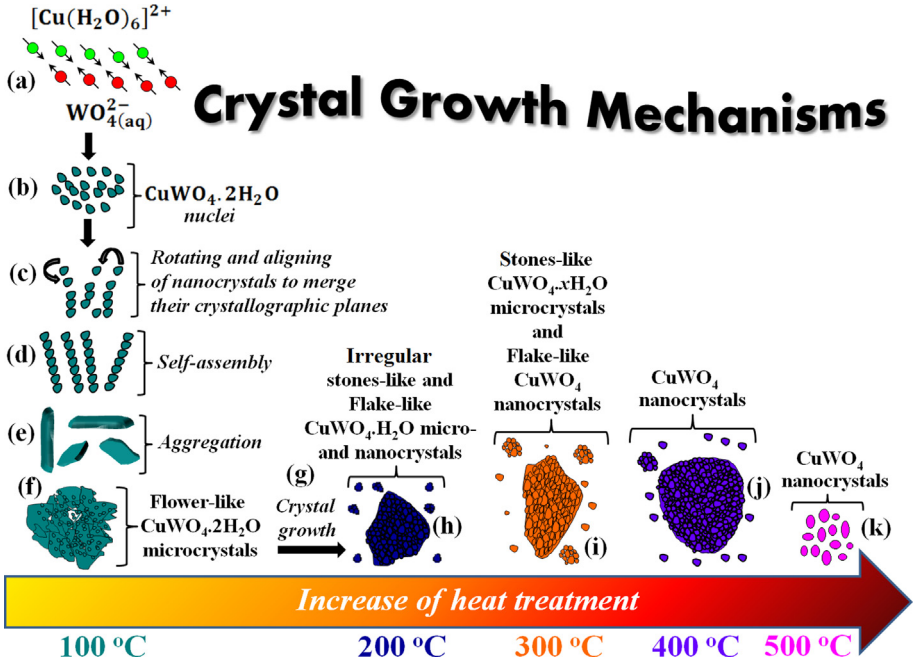

Fig. 8. Schematic representation of the growth mechanism of $CuWO_4{\cdot}2H_2O$ and $CuWO_4$ crystals obtained by the SC method: (a) reaction between complex ions; (b) appearance of the first $CuWO_4{\cdot}2H_2O$ nuclei; (c) rotation and alignment of nanocrystals, sharing common crystallographic planes; (d) self-assemble process; (e) aggregation of petal-like crystals; (f) formation of flower-like $CuWO_4{\cdot}2H_2O$ microcrystals; (g) crystal growth via heat treatment, (h) irregular stone-like $CuWO_4{\cdot}xH_2O$ microcrystals, (i) stone-like $CuWO_4{\cdot}xH_2O$ microcrystals and flake-like $CuWO_4$ nanocrystals; (j) formation of aggregated $CuWO_4$ nanocrystals; (k) crystal growth of flake-like $CuWO_4$ nanocrystals.

ping and recombination of photoinduced electrons and holes in the semiconductor. $CuWO_4$ crystals published in these papers were excited with wavelengths of 290 nm ≈ 4.276 eV and 350 nm ≈ 3.543 eV, exhibiting maximum PL emissions at 483 nm and 455 nm, respectively. Particularly, all these explanations were directly correlated to WO_4^{2-} groups (ions), but $CuWO_4$ is a crystalline solid composed of interconnected (...$[WO_6]$–$[CuO_6]$–$[WO_6]$...) clusters (Fig. 3). Therefore, in our study, we assume the distorted octahedral $[WO_6]$ clusters have an important role in the electronic transitions involving the energy levels located between the VB and CB. The existence of interconnections between octahedral $[WO_6]$ and $[CuO_6]$ clusters in the triclinic lattice indicates that any distortion caused on $[WO_6]$ clusters also promotes a slight deformation on O–Cu–O bonds ($[CuO_6]$ clusters). As O–Cu–O bonds have a covalent bond character than ionic, promoting a high degree of distortion on them. This Jahn-Teller effect, along the *z*-axis, are able to induce a symmetry break in the lattice, leading to the appearance of intermediate levels within the band gap. In Fig. 10 (a), $CuWO_4{\cdot}2H_2O$ microcrystals have a medium PL emission at 456 nm (blue) with a narrower profile in relation to other samples. Moreover, the increase of temperature at 200 °C promoted a decrease and a displacement of the PL emission for 529 nm (green region) (Fig. 10(b)) [38]. Therefore, these modifications in PL profile for samples heat treated at 100 °C and 200 °C are related to progressive removal of water molecules in $CuWO_4{\cdot}2H_2O$ crystals. The highest and widest PL spectrum was detected for the sample heat treated at 300 °C (Fig. 10(c)). This optical feature can be due to the effective contribution in electronic transitions between the intermediary energy levels arising from both $CuWO_4{\cdot}xH_2O$ and $CuWO_4$ crystals. In this case, this mixture of phases leads to different levels of short-range structural ordering in $CuWO_4$ lattice, resulting in a favorable condition for the formation of intermediate levels responsible for recombination processes (electron/hole), improving the PL behavior at room temperature. On the other hand, a significant reduction or quenching in the PL intensity was observed for single $CuWO_4$ crystals, i.e., for samples heat treated at 400 °C and 500 °C, respectively (Fig. 10(d, e)). Also, it was noted a change in the color of the powders from dark green to black (digital photos in Fig. 10(a–e)). According to black body theory [111], a hypothetical material (black) absorbs all the electromagnetic radiation. Therefore, the laser employed in the excitation process was more absorbed and not reflected in PL measurements of single $CuWO_4$ crystals. In addition, this PL behavior can be associated to other factors, such as: inhomogeneous crystal size distribution, crystallographic orientation, and morphological changes (see Supporting Information Figs. SI-2(a–i) and Fig. 3(a–j)).

4. Conclusions

In summary, $CuWO_4{\cdot}2H_2O$ and $CuWO_4$ crystals were obtained by the sonochemistry method, followed by heat treatment performed at different temperatures (from 100 °C to 500 °C) for 1 h. XRD patterns, Rietveld refinement, micro-Raman and FT-IR spectroscopies proved that $CuWO_4$ crystals crystallize in a triclinic structure with space group ($P\bar{1}$). XRD patterns revealed that the temperature of 300 °C is responsible for a phase transition from $CuWO_4{\cdot}2H_2O$ (monoclinic) to single $CuWO_4$ (triclinic). M-Raman spectra presented eighteen Raman-active vibrational modes for $CuWO_4$ nanocrystals, which are caused by external modes of distorted octahedral $[CuO_6]$ clusters and internal modes ascribed to distorted octahedral $[WO_6]$ clusters. These M-Raman spectra also showed the existence of short-range structural ordering in these crystals. FT-IR spectra detected eleven IR-active vibrational modes for $CuWO_4$ crystals, which are related to anti-symmetric, symmetric stretch, interaction forces in a chain and symmetric bending, which are present due to (O–Cu–O and O–W–O) bonds. FE-SEM images showed a dependence between the morphological aspects with the heat treatment temperature. In these micrographs, it

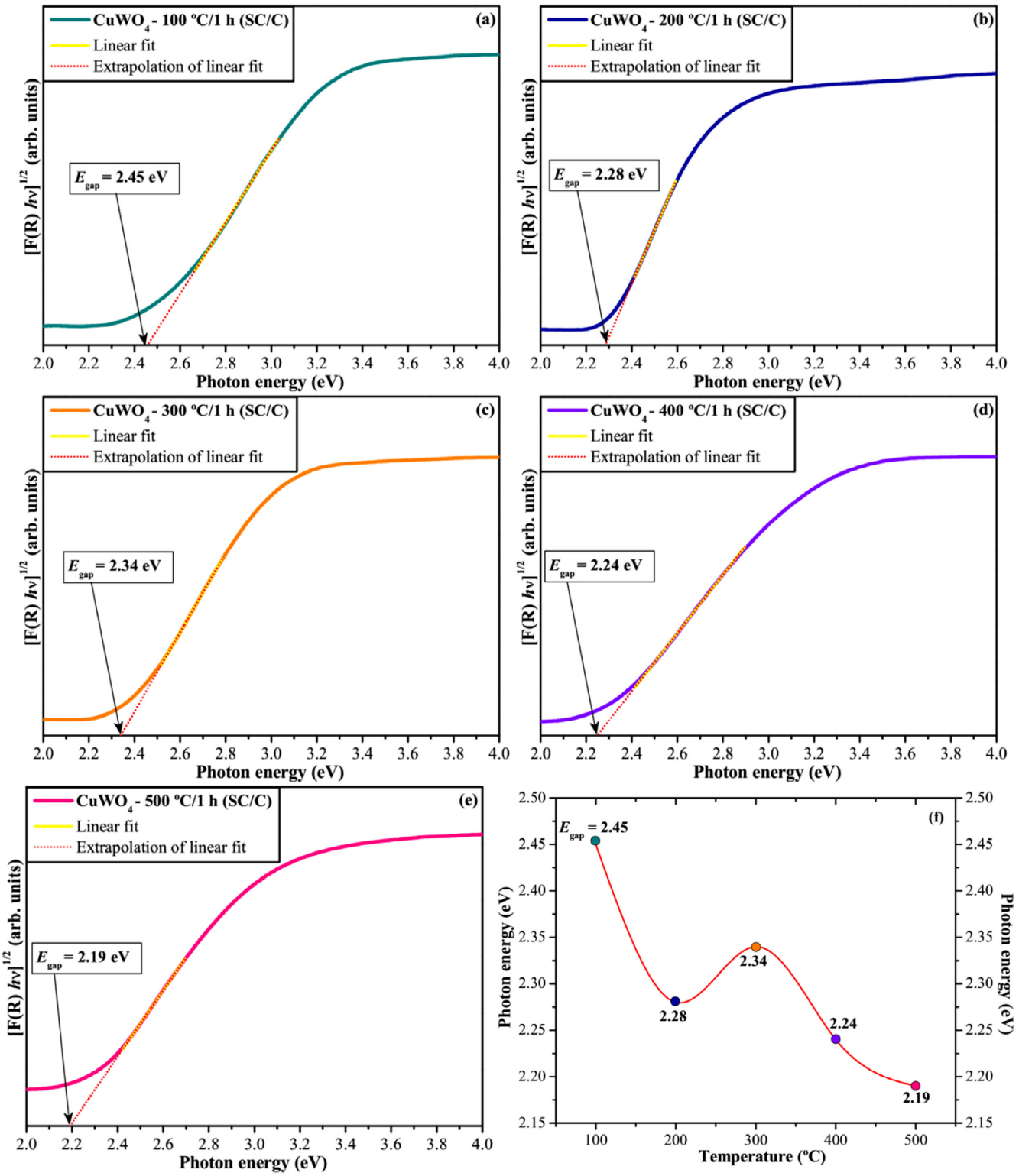

Fig. 9. UV–vis spectra of $CuWO_4$ crystals synthesized by the SC-C method and heat treated at (a) 100 °C, (b) 200 °C, (c) 300 °C, (d) 400 °C and (e) 500 °C for 1 h, and (f) E_{gap} as a function of heat treatment temperature.

was verified that $CuWO_4{\cdot}2H_2O$ crystals have irregular flower- and stone-like shaped at 100 °C and 200 °C, respectively. On the other hand, $CuWO_4$ crystals exhibited only the stone-like shaped. All these morphological shapes are composed of uncountable aggregated nanocrystals, which grew by means of self-assembly process, as observed by TEM and HR-TEM images. The decrease in E_{gap} values with the increase of the temperature was caused by the reduction of intermediary energy levels between the VB and CB. $CuWO_4$ crystals heat treated at 300 °C for 1 h exhibited the highest PL emission at room temperature. This behavior was favored due to the effective participation of intermediary energy levels arising from both $CuWO_4{\cdot}2H_2O$ and $CuWO_4$ crystals.

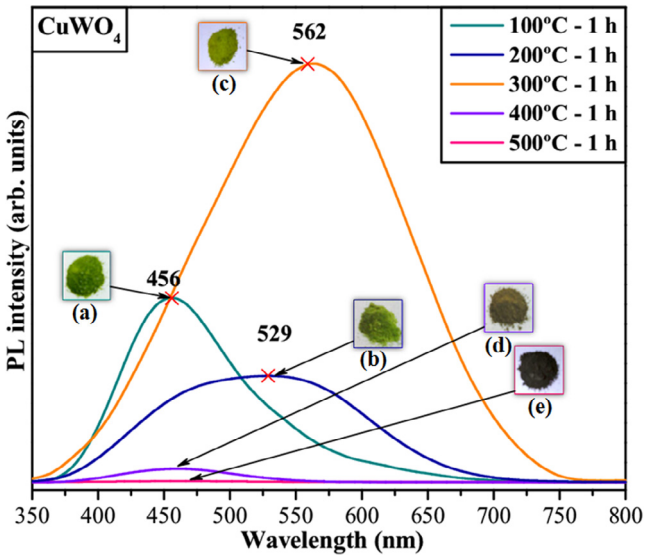

Fig. 10. PL emission spectra at room temperature of $CuWO_4$ crystals heat treated at (a) 100 °C, (b) 200 °C, (c) 300 °C, (d) 400 °C and (e) 500 °C for 1 h, respectively. Insets show the digital photos of the powders, which exhibit different colors, depending on the heat treatment temperature. (For interpretation of the references to colour in this figure legend, the reader is referred to the web version of this article.)

Acknowledgements

The authors acknowledge the financial support of the Brazilian research financing institutions: CNPq (479644/2012-8 and 304531/2013-8), FAPESP (2012/14004-5 and 2013/07296-2), and CAPES-PNPD (1268069).

Appendix A. Supplementary data

Supplementary data associated with this article can be found, in the online version, at http://dx.doi.org/10.1016/j.ultsonch.2017.03.007.

References

[1] F.L. Hess, Tungsten Minerals and Deposits, vol. 1, U.S. Government Printing Office, 1917, pp. 651–654.
[2] J.W. Mellor, A Comprehensive Treatise On Inorganic and Theoretical Chemistry, second ed., vol. 3, Longmans, Green and Co. LTD, 1928.
[3] J.J. Zhao, J.W. Li, P.L. Zhang, S.Z. Wei, G.S. Zhang, L.J. Xu, Microstructure of W-20%Cu composite powders prepared by hydrothermal synthesis combined with co-reduction method, Mater. Sci. Eng. Powder Metall. 19 (2014) 628–634.
[4] M. Douqin, X. Jingpei, L. Jiwen, W. Aiqin, W. Wenyan, L. Luoli, S. Haoliang, L. Shu, W. Fengmei, Hydrothermal synthesis of nano-sized cupric tungstate (VI) dihydrate and its synthesis mechanism, Rare Metal Mater. Eng. 43 (2014) 2917–2920.
[5] H. Zhang, J. Li, S. Wei, L. Xu, X. Ma, Process research and characterization of W coated cu nanopowder prepared by hydrothermal co-reduction technology, Chin. J. Rare Metals 39 (2015) 442–449.
[6] L. Wang, F. Ke, Q. Wang, J. Yan, C. Liu, X. Liu, Y. Li, Y. Han, Y. Ma, C. Gao, Effect of crystallization water on the structural and electrical properties of $CuWO_4$ under high pressure, Appl. Phys. Lett. 107 (2015) 201603–201607.
[7] J.G. Cheng, Y.C. Wu, Y.H. Xia, C.P. Lei, Y. Jiang, Preparation and characterization of W-Cu nanopowder by a novel homogenous coprecipitation process, J. Funct. Mater. 35 (2004), 3006–3006.
[8] M. Hashempour, H. Razavizadeh, H.R. Rezaie, D. Heidari, Effects of precursor rooted contamination in the sintering and densification behavior of thermo-chemically manufactured W-Cu nanocomposites, Internat. J. Modern Phys. B 24 (2010) 183–190.
[9] J.G. Cheng, C.P. Lei, Y. Jiang, Y.C. Wu, Y.H. Xia, Preparation of W-Cu nanopowder by homogeneous precipitation process and its sintering behavior, Chin. J. Nonferrous Met. 15 (2005) 89–93.
[10] M. Hashempour, H. Razavizadeh, H.R. Rezaie, M.T. Salehi, Thermochemical preparation of W–25%Cu nanocomposite powder through a CVT mechanism, Mater. Charact. 60 (2009) 1232–1240.
[11] M. Hashempour, H. Razavizadeh, H.R. Rezaie, M. Hashempour, M. Ardestani, Chemical mechanism of precipitate formation and pH effect on the morphology and thermochemical co-precipitation of W-Cu nanocomposite powders, Mater. Chem. Phys. 123 (2010) 83–90.
[12] M. Hashempour, H.R. Rezaie, H. Razavizadeh, M.T. Salehi, H. Mehrjoo, M. Ardestani, Investigation on fabrication of W-Cu nanocomposites via a thermochemical co-precipitation method and its consolidation behavior, J. Nano Res. 11 (2010) 57–66.
[13] M. Lazzari, L.P. Bicelli, B. Rivolta, Kinetics of the Solid State Reaction between CuO and WO_3, Zeitsch. für. Naturfor. Sect. A J. Phys. Sci. 35 (1980) 332–335.
[14] F.A. Benko, C.L. MacLaurin, F.P. Koffyberg, $CuWO_4$ and Cu_3WO_6 as anodes for the photoelectrolysis of water, Mater. Res. Bull. 17 (1982) 133–136.
[15] S.M. Montemayor, A.F. Fuentes, Electrochemical characteristics of lithium insertion in several 3D metal tungstates (MWO4, M=Mn Co, Ni and Cu) prepared by aqueous reactions, Ceram. Int. 30 (2004) 393–400.
[16] O.Y. Khyzhun, V.L. Bekenev, Y.M. Solonin, First-principles calculations and X-ray spectroscopy studies of the electronic structure of $CuWO_4$, J. Alloys Compd. 480 (2009) 184–189.
[17] S. Dey, R.A. Ricciardo, H.L. Cuthbert, P.M. Woodward, Metal-to-metal charge transfer in AWO4 (A = Mg, Mn Co, Ni, Cu, or Zn) compounds with the Wolframite structure, Inorg. Chem. 53 (2014) 4394–4399.
[18] J.B. Forsytht, C. Wilkinsont, A.I. Zvyagin, The antiferromagnetic structure of copper tungstate, $CuWO_4$, J. Phys. Cond. Matter. 3 (1991) 8433–8440.
[19] B. Lake, D.A. Tennant, R.A. Cowley, J.D. Axe, C.K. Chen, Magnetic excitations in the ordered phase of the antiferromagnetic alternating chain compound $CuWO_4$, J. Phys. Cond. Mater. 8 (1996) 8613–8634.
[20] B. Lake, R.A. Cowley, D.A. Tennant, A dimer theory of the magnetic excitations in the ordered phase of the alternating-chain compound $CuWO_4$, J. Phys. Cond. Mater. 9 (1997) 10951–10975.
[21] F. Yu, U. Schanz, E. Schmidbauer, Single crystal growth of $FeWO_4$ and $CuWO_4$, J. Crys. Growth 132 (1993) 606–608.
[22] E.L.S. Souza, C.J. Dalmaschio, M.G.R. Filho, G.E. Luz Jr., R.S. Santos, E. Longo, L.S. Cavalcante, Microscopy: Advances in Scientific Research and Education, vol. 2, 2014, pp. 894–902.
[23] W. Zhang, J. Yin, F. Min, L. Jia, D. Zhang, Q. Zhang, J. Xie, Cyclic voltammetry analysis of copper electrode performance in Na_2WO_4 solution and optical property of electrochemical synthesized $CuWO_4$ nanoparticles, J. Alloys Compd. 690 (2017) 221–227.
[24] J. Timoshenko, A. Anspoks, A. Kalinko, A. Kuzmin, Analysis of extended x-ray absorption fine structure data from copper tungstate by the reverse Monte Carlo method, Phys. Scrip. 89 (2014) 044006–044011.
[25] M.B. Naseri, A.R. Kamali, S.M.M. Hadavi, Chemical synthesis of tungsten–copper nanocomposite powder, Russian J. Inorg. Chem. 55 (2010) 167–173.
[26] S.M. Pourmortazavi, M. Rahimi-Nasrabadi, M. Khalilian-Shalamzari, H.R. Ghaeni, S.S. Hajimirsadeghi, Facile chemical synthesis and characterization of copper tungstate nanoparticles, J. Inorg. Organomet. Polym. 24 (2014) 333–339.
[27] J. Ungelenk, M. Speldrich, R. Dronskowski, C. Feldmann, Polyol-mediated low-temperature synthesis of crystalline tungstate nanoparticles MWO4 (M = Mn, Fe Co, Ni, Cu, Zn), Solid State Sci. 31 (2014) 62–69.
[28] H. Chen, Y. Xu, Photocatalytic organic degradation over W-rich and Cu-rich $CuWO_4$ under UV and visible light, RSC Adv. 5 (2015) 8108–8113.
[29] H. Chen, W. Leng, Y. Xu, Enhanced visible-light photoactivity of $CuWO_4$ through a surface-deposited CuO, J. Phys. Chem. C 118 (2014) 9982–9989.
[30] R.D. Kumar, S. Karuppuchamy, Microwave-assisted synthesis of copper tungstate nanopowder for supercapacitor applications, Ceram. Int. 40 (2014) 12397–12402.
[31] M.A.P. Almeida, L.S. Cavalcante, M.S. Li, J.A. Varela, E. Longo, Structural refinement and photoluminescence properties of $MnWO_4$ nanorods obtained by microwave-hydrothermal synthesis, J. Inorg. Organomet. Polym. 22 (2012) 264–271.
[32] M.A.P. Almeida, L.S. Cavalcante, C. Morilla-Santos, C.J. Dalmaschio, S. Rajagopal, M.S. Li, E. Longo, Effect of partial preferential orientation and distortions in octahedral clusters on the photoluminescence properties of $FeWO_4$ nanocrystals, CrystEngComm 14 (2012) 7127–7132.
[33] C. Zhang, D. Guo, C. Hu, Y. Chen, H. Liu, H. Zhang, X. Wang, Large-scale synthesis and photoluminescence of cobalt tungstate nanowires, Phys. Rev. B 87 (2013) 035416–035423.
[34] S.M.M. Zawawi, R. Yahya, A. Hassan, H.N.M.E. Mahmud, M.N. Daud, Structural and optical characterization of metal tungstates (MWO_4; M = Ni, Ba, Bi) synthesized by a sucrose-templated method, Chem. Cent. J. 7 (2013) 80–90.
[35] P. Siriwong, T. Thongtem, A. Phuruangrat, S. Thongtem, Hydrothermal synthesis, characterization, and optical properties of wolframite $ZnWO_4$ nanorods, CrystEngComm 13 (2011) 1564–1569.
[36] S. Muthamizh, R. Suresh, K. Giribabu, R. Manigandan, S.P. Kumar, S. Munusamy, L. Vijayalakshmi, A. Stephen, V. Narayanan, Solid state synthesis of copper tungstate nanoparticles and its electrochemical detection of 4-chlorophenol, AIP Confer. Proc. 1591 (2014) 508–510.
[37] D. Prasher, M. Chong, Y. Chang, P. Sarker, M.N. Huda, N. Gaillard, Development of metal tungstate alloys for photoelectrochemical water splitting, Proc. SPIE 8822 (2013) 88220E1–88220E7.
[38] D.J. Jovanovic, Lj I. Validzic, M. Mitric, J.M. Nedeljkovic, Synthesis and structural characterization of nano-sized copper tungstate particles, Acta Chim. Slov. 59 (2012) 70–74.

[39] J. Ruiz-Fuertes, A. Segura, F. Rodríguez, D. Errandonea, M.N. Sanz-Ortiz, Anomalous high-pressure Jahn-Teller behavior in $CuWO_4$, Phys. Rev. Lett. 108 (2012) 166402–166405.

[40] J. Ruiz-Fuertes, M.N. Sanz-Ortiz, J. González, F. Rodríguez, A. Segura, D. Errandonea, Optical absorption and Raman spectroscopy of $CuWO_4$, J. Phys. Conf. Ser. 215 (2010) 012048–012052.

[41] J. Ruiz-Fuertes, D. Errandonea, R. Lacomba-Perales, A. Segura, J. González, F. Rodríguez, F.J. Manjón, S. Ray, P. Rodríguez-Hernández, A. Muñoz, Z. Zhu, C.Y. Tu, High-pressure structural phase transitions in $CuWO_4$, Phys. Rev. B 81 (2010) 224115–224124.

[42] J. Ruiz-Fuertes, D. Errandonea, A. Segura, F.J. Manjón, Z. Zhu, C.Y. Tu, Growth, characterization, and high-pressure optical studies of $CuWO_4$, High Press. Res. 28 (2008) 565–570.

[43] J. Ruiz-Fuertes, A. Friedrich, J. Pellicer-Porres, D. Errandonea, A. Segura, W. Morgenroth, E. Haussühl, C.Y. Tu, A. Polian, Structure solution of the high-pressure phase of CuWO4 and evolution of the Jahn-Teller distortion, Chem. Mater. 23 (2011) 4220–4226.

[44] P.F. Schofield, S.A.T. Redfern, Ferroelastic phase transition in the sanmartinite ($ZnWO_4$)-cuproscheelite ($CuWO_4$) solid solution, J. Phys.: Condens. Matter. 4 (1992) 375–388.

[45] P.F. Schofield, C.M.B. Henderson, S.A.T. Redfern, G. van der Laan, Cu 2*p* absorption spectroscopy as a probe for the site occupancy of $(Zn_xCu_{1-x})WO_4$ solid solution, Phys. Chem. Minerals 20 (1993) 375–381.

[46] P.F. Schofield, J.M. Charnock, G. Cressey, C.M.B. Henderson, An EXAFS study of cation site distortions through the *P*2/c-*P*1 phase transition in the synthetic cuproscheelite-sanmartinite solid solution, Miner. Magaz. 58 (1994) 185–199.

[47] S.A.T. Redfern, P.F. Schofield, Order parameter saturation (plateau effect) as a function of composition in the sanmartinite ($ZnWO_4$) – cuproscheelite ($CuWO_4$) solid solution, Phase Trans. 59 (1996) 25–38.

[48] M. Imada, A. Fujimori, Y. Tokura, Metal-insulator transitions, Rev. Mod. Phys. 70 (1998) 1039–1263.

[49] P. Patureau, M. Josse, R. Dessapt, J.Y. Mevellec, F. Porcher, M. Maglione, P. Deniard, C. Payen, Incorporation of Jahn–Teller Cu^{2+} ions into magnetoelectric multiferroic $MnWO_4$: structural, magnetic, and dielectric permittivity properties of $Mn_{1-x}Cu_xWO_4$ ($x \leq 0.25$), Inorg. Chem. 54 (2015) 10623–10631.

[50] J.P. Doumerc, J. Hejtmanek, J.P. Chaminade, M. Pouchard, M. Krussanova, A photoelectrochemical study of $CuWO_4$ single crystals, Phys. Status Solidi A 82 (1984) 285–294.

[51] K.J. Pyper, J.E. Yourey, B.M. Bartlett, Reactivity of $CuWO_4$ in photoelectrochemical water oxidation is dictated by a midgap electronic state, J. Phys. Chem. C 117 (2013) 24726–24732.

[52] M.A. Halcrow, Interpreting and controlling the structures of six-coordinate copper(II) centres – When is a compression *really* a compression?, Dalton Trans 1 (2003) 4375–4384.

[53] P. ReddyPrasad, E.B. Naidoo, Ultrasonic synthesis of high fluorescent C-dots and modified with $CuWO_4$ nanocomposite for effective photocatalytic activity, J. Mol. Struct. 1098 (2015) 146–152.

[54] T. Montini, V. Gombac, A. Hameed, L. Felisari, G. Adami, P. Fornasiero, Synthesis, characterization and photocatalytic performance of transition metal tungstates, Chem. Phys. Lett. 30 (2010) 113–119.

[55] P. Schmitt, N. Brem, S. Schunk, C. Feldmann, Polyol-mediated synthesis and properties of nanoscale molybdates/tungstates: Color, luminescence, catalysis, Adv. Funct. Mater. 21 (2011) 3037–3046.

[56] B. Schwarz, H. Ehrenberg, H. Weitzel, A. Senyshyn, B. Thybusch, M. Knapp, G.J. McIntyred, H. Fuess, Crystal chemistry, structure and magnetic properties of the $Cu(Mo_xW_{1-x})O_4$ solid solution series, Philos. Mag. 88 (2008) 1235–1258.

[57] B.C. Schwarz, H. Ehrenberg, H. Weitzel, H. Fuess, Investigation on the influence of particular structure parameters on the anisotropic spin-exchange interactions in the distorted wolframite-type oxides $Cu(Mo_xW_{1-x})O_4$, Inorg. Chem. 46 (2007) 378–380.

[58] H.J. Koo, M.H. Whangbo, Spin dimer analysis of the anisotropic spin exchange interactions in the distorted Wolframite-Type oxides $CuWO_4$, $CuMoO_4$-III, and $Cu(Mo_{0.25}W_{0.75})O_4$, Inorg. Chem. 40 (2001) 2161–2169.

[59] J.E. Yourey, J.B. Kurtz, B.M. Bartlett, Structure, optical properties, and magnetism of the full $Zn_{1-x}Cu_xWO_4$ ($0 \leq x \leq 1$) composition range, Inorg. Chem. 51 (2012) 10394–10401.

[60] Y. Tang, N. Rong, F. Liu, M. Chu, H. Dong, Y. Zhang, P. Xiao, Enhancement of the photoelectrochemical performance of $CuWO_4$ films for water splitting by hydrogen treatment, Appl. Surf. Sci. 361 (2016) 133–140.

[61] D. Bohra, W.A. Smith, Improved charge separation via Fe-doping of copper tungstate photoanodes, Phys. Chem. Chem. Phys. 17 (2015) 9857–9866.

[62] A. Martínez-García, V.K. Vendra, S. Sunkara, P. Haldankar, J. Jasinski, M.K. Sunkara, Tungsten oxide-coated copper oxide nanowire arrays for enhanced activity and durability with photoelectrochemical water splitting, J. Mater. Chem. A 1 (2013) 15235–15241.

[63] M. Valenti, D. Dolat, G. Biskos, A. Schmidt-Ott, W.A. Smith, Enhancement of the photoelectrochemical performance of $CuWO_4$ thin films for solar water splitting by plasmonic nanoparticle functionalization, J. Phys. Chem. C 119 (2015) 2096–2104.

[64] F. Zhan, J. Li, W. Li, Y. Liu, R. Xie, Y. Yang, Y. Li, Q. Chen, In situ formation of $CuWO_4/WO_3$ heterojunction plates array films with enhanced photoelectrochemical properties, Int. J. Hydrogen Energy 40 (2015) 6512–6520.

[65] N. Gaillard, Y. Chang, A. DeAngelisa, S. Higginsa, A. Braun, A nanocomposite photoelectrode made of 2.2 eV band gap copper tungstate ($CuWO_4$) and multi-wall carbon nanotubes for solar-assisted water splitting, Int. J. Hydrogen Energy 38 (2013) 3166–3176.

[66] J.E. Yourey, B.M. Bartlett, Electrochemical deposition and photoelectrochemistry of $CuWO_4$, a promising photoanode for water oxidation, J. Mater. Chem. 21 (2011) 7651–7660.

[67] J.C. Hill, K.S. Choi, Synthesis and characterization of high surface area $CuWO_4$ and Bi_2WO_6 electrodes for use as photoanodes for solar water oxidation, J. Mater. Chem. A 1 (2013) 5006–5014.

[68] S.K. Pilli, T.G. Deutsch, T.E. Furtak, L.D. Brown, J.A. Turner, A.M. Herring, $BiVO_4/CuWO_4$ heterojunction photoanodes for efficient solar driven water oxidation, Phys. Chem. Chem. Phys. 15 (2013) 3273–3278.

[69] R. Bharati, R. Shanker, R.A. Singh, Electrical transport properties of $CuWO_4$, Pramana 14 (1980) 449–454.

[70] S.M. Pourmortazavi, M. Rahimi-Nasrabadi, Y. Fazli, M. Mohammad-Zadeh, Taguchi method assisted optimization of electrochemical synthesis and structural characterization of copper tungstate nanoparticles, Int. J. Refract. Met. Hard Mater. 51 (2015) 29–34.

[71] A. Kuzmin, A. Kalinko, R.A. Evarestov, Ab initio LCAO study of the atomic, electronic and magnetic structures and the lattice dynamics of triclinic $CuWO_4$, Acta Mater. 61 (2013) 371–378.

[72] M.V. Lalic, Z.S. Popovic, F.R. Vukajlovic, Ab initio study of electronic, magnetic and optical properties of $CuWO_4$ tungstate, Comput. Mater. Sci. 50 (2011) 1179–1186.

[73] P. Sarker, D. Prasher, N. Gaillard, M.N. Huda, Predicting a new photocatalyst and its electronic properties by density functional theory, J. Appl. Phys. 114 (2013) 133508–133517.

[74] V.V. Atuchin, I.B. Troitskaia, O.Y. Khyzhun, V.L. Bekenev, Y.M. Solonin, Electronic properties of h-WO_3 and $CuWO_4$ nanocrystals as determined from X-ray spectroscopy and first-principles band-structure calculations, Inter. J. Appl. Phys. Mathem. 1 (2011) 19–23.

[75] J.C. Hill, Y. Ping, G.A. Galli, K.S. Choi, Synthesis, photoelectrochemical properties, and first principles study of n-type CuW1-*x*MoxO_4 electrodes showing enhanced visible light absorption, Energy Environ. Sci. 6 (2013) 2440–2446.

[76] R.F. Gonçalves, L.S. Cavalcante, I.C. Nogueira, E. Longo, M.J. Godinho, J.C. Sczancoski, V.R. Mastelaro, I.M. Pinatti, I.L.V. Rosa, A.P.A. Marques, Rietveld refinement, cluster modelling, growth mechanism and photoluminescence properties of $CaWO_4:Eu^{3+}$ microcrystals, CrystEngComm 17 (2015) 1654–1666.

[77] S.N. Guin, D. Sanyal, K. Biswas, The effect of order–disorder phase transitions and band gap evolution on the thermoelectric properties of AgCuS nanocrystals, Chem. Sci. 7 (2016) 534–543.

[78] L. Kihlborg, E. Gebert, $CuWO_4$, a distorted Wolframite-type structure, Acta Cryst. Sec. B 26 (26) (1970) 1020–1026.

[79] H.M. Rietveld, Line profiles of neutron powder-diffraction peaks for structure refinement, Acta Crystallogr. 22 (1967) 151–152.

[80] H.M. Rietveld, A profile refinement method for nuclear and magnetic structures, J. Appl. Crystallogr. 2 (1969) 65–71.

[81] A.C. Larson, R.B. Von Dreele, General Structure Analysis System (GSAS), National Laboratory, Los Alamos, 2001.

[82] P. Thompson, D.E. Cox, J.B. Hastings, Rietveld refinement of Debye-Scherrer synchrotron X-ray data from Al2O3, J. Appl. Cryst. 20 (1987) 79–83.

[83] L.W. Finger, D.E. Cox, A.P. Jephcoat, A correction for powder diffraction peak asymmetry due to axial divergence, J. Appl. Cryst. 27 (1994) 892–900.

[84] P.W. Stephens, Phenomenological model of anisotropic peak broadening in powder diffraction, J. Appl. Cryst. 32 (1999) 281–289.

[85] P.F. Schofield, K.S. Knight, S.A.T. Redfern, G. Cressey, Distortion characteristics across the structural phase transition in $(Cu_{1-x}Zn_x)WO_4$, Acta Cryst. Sec. B 53 (1997) 102–112.

[86] K. Momma, F. Izumi, VESTA: a three-dimensional visualization system for electronic and structural analysis, J. Appl. Crystallogr. 41 (2008) 653–658.

[87] K. Momma, F. Izumi, VESTA 3 for three-dimensional visualization of crystal, volumetric and morphology data, J. Appl. Crystallogr. 44 (2011) 1272–1276.

[88] L.S. Cavalcante, E. Moraes, M.A.P. Almeida, C.J. Dalmaschio, N.C. Batista, J.A. Varela, E. Longo, M. Siu Li, J. Andres, A. Beltran, A combined theoretical and experimental study of electronic structure and optical properties of β-$ZnMoO_4$ microcrystals, Polyhedron 54 (2013) 13–25.

[89] I.M. Pinatti, I.C. Nogueira, W.S. Pereira, P.F.S. Pereira, R.F. Gonçalves, J.A. Varela, E. Longo, I.L.V. Rosa, Structural and photoluminescence properties of Eu^{3+} doped α-Ag_2WO_4 synthesized by the green coprecipitation methodology, Dalton Trans. 44 (2015) 17673–17685.

[90] R.L. Frost, L. Duong, M. Weier, Raman microscopy of selected tungstate minerals, Spectrochim. Acta Part A 60 (2004) 1853–1859.

[91] T.T. Basiev, A.A. Sobol, Y.K. Voronko, P.G. Zverev, Spontaneous Raman spectroscopy of tungstate and molybdate crystals for Raman lasers, Opt. Mater. 15 (2000) 205–2016.

[92] R.K. Selvan, A. Gedanken, The sonochemical synthesis and characterization of Cu1−xNixWO4 nanoparticles/nanorods and their application in electrocatalytic hydrogen evolution, Nanotechnology 20 (2009) 105602–105608.

[93] L.S. Cavalcante, M.A.P. Almeida, W. Avansi Jr., R.L. Tranquilin, E. Longo, N.C. Batista, V.R. Mastelaro, M. Siu Li, Cluster coordination and photoluminescence properties of α–Ag_2WO_4 microcrystals, Inorg. Chem. 51 (2012) 10675–10687.

[94] J. Ruiz-Fuertes, J. Pellicer-Porres, A. Segura, P. Rodríguez-Hernández, A. Muñoz, Lattice and electronic contributions to the refractive index of $CuWO_4$, J. Appl. Phys. 116 (2014) 103706–103711.
[95] H. Ramezanalizadeh, F. Manteghi, Design and development of a novel $BiFeO_3$/$CuWO_4$ heterojunction with enhanced photocatalytic performance for the degradation of organic dyes, J. Photochem. Photobiol. A Chem. 338 (2017) 60–71.
[96] A. Anspoks, A. Kalinko, J. Timoshenko, A. Kuzmin, Local structure relaxation in nanosized tungstates, Solid State Commun. 183 (2014) 22–26.
[97] G.M. Clark, W.P. Doyle, Infra-red spectra of anhydrous molybdates and tungstates, Spectrochim. Acta 22 (1966) 1441–1447.
[98] A.W. Sleight, High pressure CuMoO4, Mater. Res. Bull. 8 (1973) 863–866.
[99] L. Liang, H. Liu, Y. Tian, Q. Hao, C. Liu, W. Wang, X. Xie, Fabrication of novel $CuWO_4$ hollow microsphere photocatalyst for dye degradation under visible-light irradiation, Mater. Lett. 182 (2016) 302–304.
[100] S.M. Hosseinpour-mashkani, A. Sobhani-Nasa, Simple synthesis and characterization of copper tungstate nanoparticles: investigation of surfactant effect and its photocatalyst application, J. Mater. Sci. Mater. Electron. 27 (2016) 7548–7553.
[101] W. Ye, F. Chen, F. Zhao, N. Han, Y. Li, $CuWO_4$ nanoflake array-based single-junction and heterojunction photoanodes for photoelectrochemical water oxidation, ACS Appl. Mater. Interf. 8 (2016) 9211–9217.
[102] R.D. Kumar, Y. Andou, M. Sathish, S. Karuppuchamy, Synthesis of nanostructured Cu-WO_3 and $CuWO_4$ for supercapacitor applications, J. Mater. Sci. Mater. Electron. 27 (2016) 2926–2932.
[103] X. Xie, M. Liu, C. Wang, L. Chen, J. Xu, Y. Cheng, H. Dong, F. Lu, W.H. Wang, H. Liu, W. Wang, Efficient photo-degradation of dyes using $CuWO_4$ nanoparticles with electron sacrificial agents: a combination of experimental and theoretical exploration, RSC Adv. 6 (2016) 953–959.
[104] E. Limpert, W. Stahel, M. Abbt, Log-normal distributions across the sciences: keys and clues, BioScience 51 (2001) 341–352.
[105] P. Kubelka, F. Munk, Ein Beitrag zur optik der farbanstriche, Z. Fur Tech. Phys. 12 (1931) 593–601.
[106] M.L. Myrick, M.N. Simcock, M. Baranowski, H. Brooke, S.L. Morgan, J.N. Mccutcheon, The Kubelka-Munk diffuse reflectance formula revisited, Appl. Spectrosc. Rev. 46 (2011) 140–165.
[107] R.A. Smith, Semiconductors, second ed., vol. 1, Cambridge University Press, London, 1978.
[108] R. Lacomba-Perales, J. Ruiz-Fuertes, D. Errandonea, D. Martınez-Garcıa, A. Segura, Optical absorption of divalent metal tungstates: correlation between the band-gap energy and the cation ionic radius, Europhys. Lett. 83 (2008) 37002–37011.
[109] E. Longo, D.P. Volanti, V.M. Longo, L. Gracia, I.C. Nogueira, M.A.P. Almeida, A. N. Pinheiro, M.M. Ferrer, L.S. Cavalcante, J. Andres, Toward an understanding of the growth of ag filaments on α-Ag_2WO_4 and their photoluminescent properties: a combined experimental and theoretical study, J. Phys. Chem. C 118 (2014) 1229–1239.
[110] R.A. Roca, J.C. Sczancoski, I.C. Nogueira, M.T. Fabbro, H.C. Alves, L. Gracia, L.P. S. Santos, C.P. de Sousa, J. Andrés, G.E. Luz Jr., E. Longo, L.S. Cavalcante, Facet-dependent photocatalytic and antibacterial properties of α-Ag_2WO_4 crystals: combining experimental data and theoretical insights, Catal. Sci. Technol. 5 (2015) 4091–4107.
[111] M. Massoud, Blackbody Radiation. Engineering Thermofluids: Thermodynamics, Fluid Mechanics, and Heat Transfer, Springer-Verlag, Berling, 2005.